**Solid Freeform Fabrication 2022: Proceedings of the 33rd Annual International Solid Freeform Fabrication Symposium – An Additive Manufacturing Conference**
**Reviewed Paper**

# X-RAY ANALYSIS OF MAGNETICALLY INDUCED ADDITIVE MANUFACTURING

R. Sellers*, C. McCullough*, E. Gonzalez*, A. Light*, S. Wolff*, and H. Wang*

*Department of Industrial and Systems Engineering, Texas A&M University, College Station, Tx 77840

*Keywords: Additive Manufacturing; Ti64; SS 316L; Laser Powder Bed Fusion; X-ray Analysis; Keyhole; Marangoni Flow; Magnetic Fields*

## Abstract

Through advancements in technology over the last several years, additive manufacturing has become increasingly mainstream in the manufacturing process. Additive manufacturing has several traits which would theoretically make it superior to traditional subtractive manufacturing techniques. While this ability to manufacture complex parts is certainly applicable to the external structure, additive manufacturing will allow for control over the internal structure of a part as well. From this, porous components can be created which match desired mechanical properties somewhat independently of the material actually used for manufacturing. However, many of these advancements require further refinement of the additive manufacturing processes intrinsic to them. One of the techniques suggested as a method of improving additive manufacturing processes is the incorporation of magnets into the manufacturing process. These magnets are used to direct the flow of the melted metal with more precision. Experiments were conducted in order to evaluate the effects of the introduction of magnets on parts printed using Laser Powder Bed Fusion. Stainless steel 316L, a relatively cheap and easy to print steel, was printed onto a Ti64 substrate using both spot welding and line scanning. It was observed that magnets had an effect on the melt pool and the keyhole depth through an analysis of the spot welding. Additionally, the various magnets also changed the flow of particles in the melted areas generated through line scanning. While quantifying the magnetic fields' effects will require additional research and time, there is strong evidence that they could be a viable solution to increasing additive manufacturing's precision.

## Introduction

The importance of additive manufacturing (AM) as an alternative to modern manufacturing techniques has grown significantly over the last several years [1, 2]. AM is a manufacturing method where material is added in a layer-by-layer manner in order to "print" a three-dimensional part. There are many different ways to add material layers with techniques such as stereolithography, fused deposition modeling, binder jetting, powder bed fusion, and many others. In the case of this powder bed fusion technique, each layer, after being placed on a base material, is melted using a laser to create a solid part. This technique is increasingly applicable to industries such as aerospace, biomedical, dental, and nuclear. While AM is certainly still being researched and optimized, further advancements could lead to AM creating parts that are superior to traditional methods in both mechanical properties and manufacturing efficiency. However, AM currently lacks the precision necessary to achieve these improvements. One of the suggested methods for improving these flaws is the implementation of magnets as a method of guiding the material to the desired location. The effects of including magnets in the manufacturing process is where we focused our research. We explored the effects of two styles of magnets, a long rectangular magnet and circular ring magnet. Additionally, two printing material types were explored: Ti-6Al-4V (Ti64), a popular titanium alloy with excellent material properties, and stainless steel 316L (SS316), a relatively cheap and easy to manufacture metal [3]. From our experimentation we collected data on several important aspects of the printing process including: the depth and width of the melt pool, the way pores form in the part, the structure of the metal at a microscopic level, and the flow of particles throughout the material.

## Methods

Our parts were printed using Laser Powder Bed Fusion (LPBF) at Argonne National Laboratory (ANL). LPBF is currently one of the most popular techniques for AM [2]. This process involves distributing powder evenly over a substrate before the laser melts desired areas. A new powder layer is distributed once the previous layer has been completed after the build platform has been lowered slightly. This process continues until the part or sample is finished. For the purposes of our experiments, magnets were placed on both sides of the substrate, with the print area being between the two magnets. **Figure 1** shows the experimental setup using the LPBF technique. Two different substrates were used for this experiment. Ti64 was used for line scan experiments, and SS316 was used for the spot welding experiments. The line scan experiments involved the laser moving from a starting point to an end point in a straight line while the spot welding was a stationary laser turned on for a specified length. During the line scan experiments, Tungsten (W) particles were mixed in with the powder layer to allow for flow tracking from the x-ray camera. **Table 1** shows the process parameters for the different experiments. The maximum power for the laser was specified at 526 W.

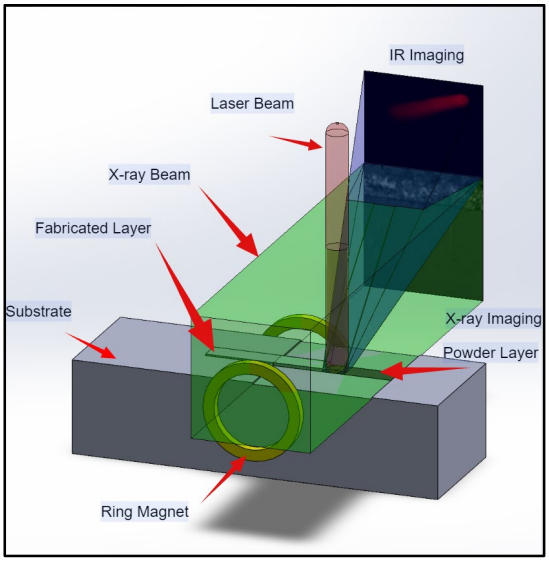


**Figure 1.** LPBF setup for printing and imaging at Argonne National Laboratory

**Table 1.** Process Parameters

| Experiment | Material | Laser Power % | Dwell Time/Scan Speed | Magnet |
|---|---|---|---|---|
| 11 | 316L SS, 0.038 mm | 23 | 1500 µs – spot weld | Long magnet |
| 58 | 316L SS, 0.038 mm | 23 | 1500 µs – spot weld | No magnet |
| 157 | 316L SS, 0.038 mm | 23 | 1500 µs – spot weld | Ring magnet |
| 173 | Ti with W powder mix | 35 | 300 m/s – line scan | Long magnet |
| 189 | Ti with W powder mix | 35 | 300 m/s – line scan | No magnet |

*X-ray imaging*

During experimentation, x-ray images were taken of the process. These images had to be processed using ImageJ, an image processing software, prior to data collection [4]. This processing involves subtracting an image from the group of images, as well as changing parameters like brightness and contrast in order to generate a clearer image. An example of images before and after processing can be seen in **Figure 2.** Once the images were processed, the melt pool widths and key hole depths could be measured using the tools in ImageJ. This returned a value in pixels, which were then converted to micrometers (μm).

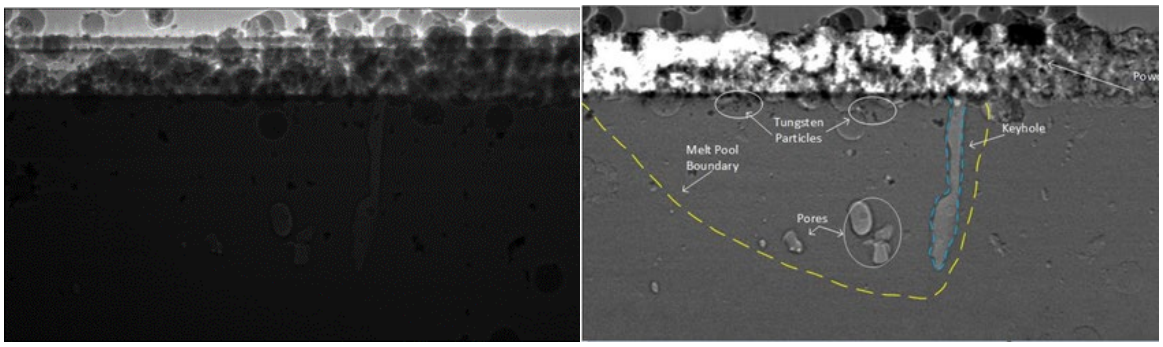


**Figure 2.** a) pre-processed, raw x-ray image; b) processed and annotated image of line scan experiment

*Magnetic field modeling*

Some of the magnets used in the experiments consisted of long, short, and ring shapes. Each magnet was of grade N52, supplied by K&J Magnetics. **Figure 3** shows two different models of accurate magnetic field simulations. The first model, done in Finite Element Model Magnetics (FEMM) shows the flux density of the magnetic field. From this model it is clear that the fields are much more dense closer to the magnet, and at a certain distance the magnets lose all effectiveness. The second model, done in ANSYS Mechanical, shows the effect the field has on the SS316 substrate in a 3D environment. These models were done to understand how the magnetic fields were displaced around the stainless steel and how they should theoretically cause the direction of flow to change. No data or conclusions were generated from these simulations.

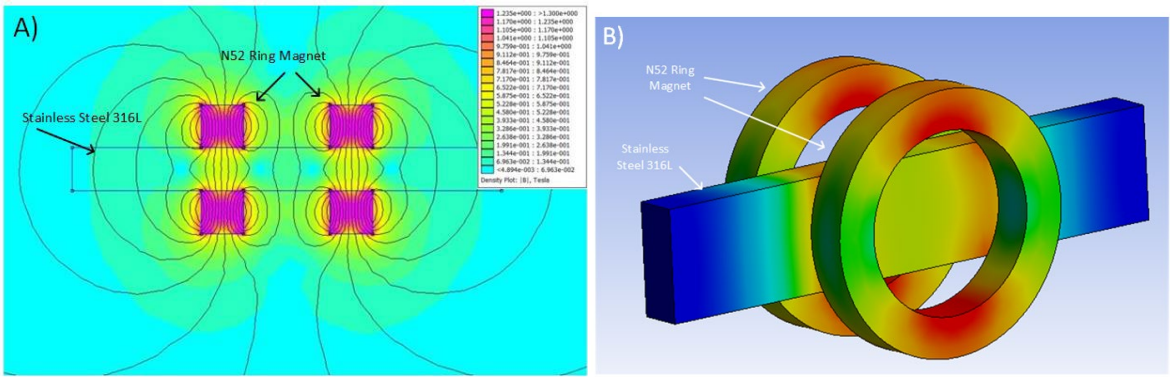


**Figure 3.** a) FEMM model with ring magnet setup; b) ANSYS Mechanical Magnetostatic simulation to visualize magnetic field effect on SS316L, where blue to red is a measure of low to high relative flux density strength, respectively

## Results

**Figure 4** is annotated to show the different characteristics of the melt pool such as the substrate, melt pool boundary, keyhole depth, and sub-melt pool layer. The two rows in the figure are from experiment 11 (top row) and experiment 157 (bottom row), both operating at the same parameters of laser power, dwell time, and

material. The only difference between the two is the magnet that was used. Experiment 11 used a long magnet, and experiment 157 used a ring magnet.

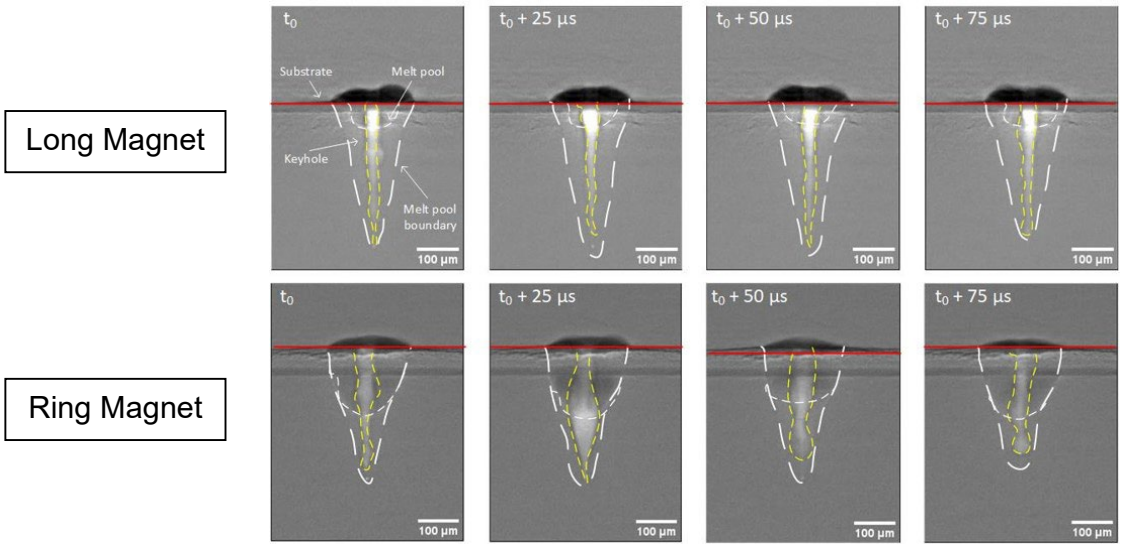


**Figure 4.** Comparison of keyhole depths due to magnetic field distributions. Top row (exp 11) contains a long magnet while the bottom row (exp 157) is affected by a ring magnet

From the image, it can be seen that the ring magnet has a greater effect on the sub-melt pool layer, which is denoted by the smaller white line within the melt pool boundary layer. No statistical analysis or further study was performed on this observation, but it can be seen that the sub-melt pool depth increased with the ring magnet from visual data. This sub-melt pool boundary is from the camera only being able to show a 2D area of the 3D melt pool. It can also be seen that the keyhole depth for the ring magnet is slightly shorter than the long magnet, indicating a possible qualitative change.

*Keyhole Depth*

The first measurement made is with the keyhole depth from experiments 11, 58, and 157. Exp 58 contains the same parameters as 11 and 157, except it does not utilize a magnetic field distribution. Keyhole depth over the dwell time of the experiment can be seen in **Figure 5**, which follows a lognormal curve of the measurements. From the graph, along with **Table 1,** a clear depiction between the variance of the heights due to magnetic fields can be seen. The experiment without a magnet presented the highest variance and mean, while the experiment with a ring magnet showed the lowest variance and mean. This result shows that the ring's magnetic field distribution reduces the fluctuation in keyhole depth.

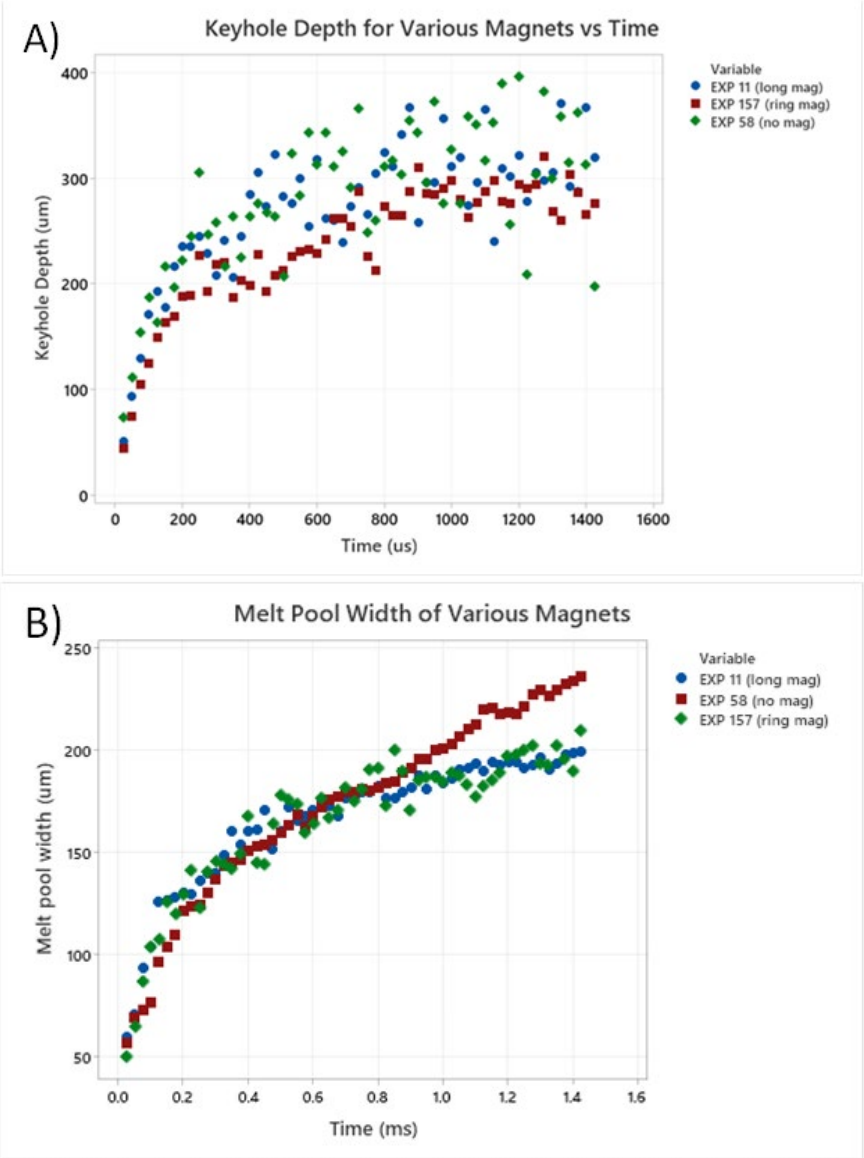


**Figure 5.** a) Comparison of keyhole depths due to various magnetic fields; b) melt pool width measurements with varying magnetic fields

Along with the visual representation from the graph, ANOVA and Tukey tests were performed to test for differences in means and confidence intervals. From the tests, it was found that exp 157 is statistically significant from p-values and grouping methods. These tests can be quantified in **Table 2**. This can be seen by looking at the p-values and confidence intervals. If the p-value is less than 0.05, or the confidence interval does not include zero, they are statistically significant. Both combinations of experiments with 157 show a p-value of 0.013 and 0.001, respectively. Grouping is another way to measure statistical significance, where if groups share a letter, they are not statistically different. In this case, the means for exp 11 and 58 share the same letter while 157 does not.

*Melt Pool Width*

The melt pool widths were also measured for the same experiments. Based on the graph in **Figure 5**, the presence of a magnet lowers the melt pool width after about 1 ms. Prior to 1 ms, widths for all experiments are about the same with minor fluctuations. After averaging the data, the presence of a magnet lowered the average melt pool width.

From **Table 2**, it can be seen that although the variance is significantly reduced by ring magnets, the average widths are around the same. In fact, the average melt pool width for the ring magnet experiment was greater than the long magnet, but still less than no magnet. ANOVA and Tukey tests were also performed for the melt pool widths through Minitab. By the aforementioned analysis standards, it was found that neither the ring magnet or the long magnet caused the experiments to be statistically different from the experiment without a magnet, shown numerically in **Table 3**. These p-values were found to be relatively high, suggesting that the magnets are not close to making a difference in the measurements.

**Table 2.** Measurements of Keyhole Depths and Melt Pool Widths

| Measurement | Experiment | Average (μm) | Variance ($\sigma^2$) |
|---|---|---|---|
| Keyhole Depth | 11 (Long Magnet) | 271.71 | 4001.11 |
| | 58 (No Magnet) | 282.60 | 4800.05 |
| | 157 (Ring Magnet) | 237.35 | 3467.69 |
| Melt Pool Width | 11 (Long Magnet) | 150.14 | 2155.84 |
| | 58 (No Magnet) | 172.48 | 2123.66 |
| | 157 (Ring Magnet) | 165.66 | 1209.11 |

**Table 3.** ANOVA and Tukey Test Results

| Measurement | Experiment Combination | Tukey Adjusted P-value | 95% Confidence Interval | F-Value |
|---|---|---|---|---|
| Keyhole Depth | Exp 58 - Exp 11 | 0.635 | (-17.4, 39.2) | 7.77 |
| | Exp 157 - Exp 11 | 0.013 | (-62.7, -6.1) | |
| | Exp 157 - Exp 58 | 0.001 | (-73.5, -17.0) | |
| Melt Pool Width | Exp 58 - Exp 11 | 0.669 | (-10.73, 22.90) | 0.55 |
| | Exp 157 - Exp 11 | 0.994 | (-17.55, 16.08) | |
| | Exp 157 - Exp 58 | 0.604 | (-23.64, 9.99) | |

*Melt Flow Dynamics*

An important concept in fluids is the Marangoni Effect, which takes place when there is a surface tension gradient, or change, between two phases that ultimately affects the pressures within the fluids. This flow is affected by temperature along the interface, which is why it occurs within additive manufacturing. The surface tension can be found by using **Eq. 1**. However due to lack of certain data captured, the surface tension was experimentally estimated to be -4.81x10$^{-4}$ at 1700 ℃ [5, 6, 7]. This equation does not directly account for the magnetic field impacting the melt pool, but we are able to use it and visualize why the values would be different than an experiment without a magnetic field.

$$\frac{\partial\sigma}{\partial T} = -A - \Gamma_s \cdot R \cdot ln(1 + \alpha_s \cdot k_1 \cdot exp(-\frac{\Delta H_0}{RT})) - \frac{\alpha_s \cdot \Gamma_s \cdot \Delta H_0 \cdot k_1 \cdot exp(-\frac{\Delta H_0}{RT})}{T(1+\alpha_s \cdot k_1 \cdot exp(-\frac{\Delta H_0}{RT})} \quad \text{(Eq. 1)}$$

Marangoni Flow can be calculated with **Eq. 2;** where L is the length of the melt pool, ΔT is the temperature, μ is the viscosity, and α is the thermal diffusivity. Using this equation**,** we found the Marangoni flow to be approximately 12.698, which indicates a relatively low Marangoni flow between the Ti64 and the Tungsten trackers in the melt pool as opposed to other studies done without magnetic interference [8, 9]. The tungsten particles were mixed in with the powder layer and were chosen due to the higher melting temp. One of the possible causes for the difference in calculation vs. experimental measurements could be from the magnetic field, which would cause the pressures within the substrate to vary. The magnetic field in combination with laser power and scan speed, along with any sort of additives can affect the flow back behind the laser and the Marangoni number. We can use the Marangoni Flow value to observe the velocity of the particles to understand why they behave certain ways within the molten liquid layers.

$$Ma = -\frac{\partial\sigma}{\partial T} \cdot \frac{L\Delta T}{\mu\alpha} \quad \text{(Eq. 2)}$$

The last important concept to look at is settling velocity and how it is affected by the surrounding magnetic fields. Without the addition of the magnetic field, settling velocity can be found for certain particles by using **Eq 3**:

$$v_p = \frac{\rho_p - \rho_f}{\gamma\mu_f} g d_p^2 \quad \text{(Eq. 3)}$$

where $\rho_p$, is the mass density of the tungsten particle $\rho_f$ is the mass density of the fluid, g is the gravitational constant, $\mu_f$ is the dynamic viscosity, $d_p$ is the diameter of the tungsten particle, and $\gamma$ is the coefficient that depends on the fluid and particle velocity (12 in this case for solid particles) [6, 10]. We calculated the theoretical velocities for 3 locations within the substrate, which can be compared with the experimentally measured values in **Table 4.** Zone 1 is arbitrarily defined as the top of the melt pool, zone 2 is the middle, and zone 3 is the area near the bottom of the keyhole. These locations can be seen in **Figure 6**, along with a graph of the respective velocities. This table shows the different particles for experiment 173, which is a line scanning process with a long magnet. It can be seen that the measured velocities are a few magnitudes higher than the theoretical velocities. One explanation for this is the effect of the magnetic fields, which could cause the particles to accelerate or decelerate in certain directions and in non-behavioral fashions. This is important to understand as future experiments could utilize magnets to help mix powders evenly and more efficiently within the substrate, rather than just on the surface. These particles were tracked using a plugin named *Trackmate* within the ImageJ application [11].

**Table 4.** Comparison Between Experimental and Theoretical Velocities for Experiment 173

| Particle Position | Settling Velocity (m/s) | Measured Velocity (m/s) |
|---|---|---|
| Top | $6.49 \times 10^{-4}$ | $6.43 \times 10^{-2}$ |
| Middle | $4.45 \times 10^{-4}$ | $3.15 \times 10^{-2}$ |
| Bottom | $5.22 \times 10^{-4}$ | $3.18 \times 10^{-2}$ |

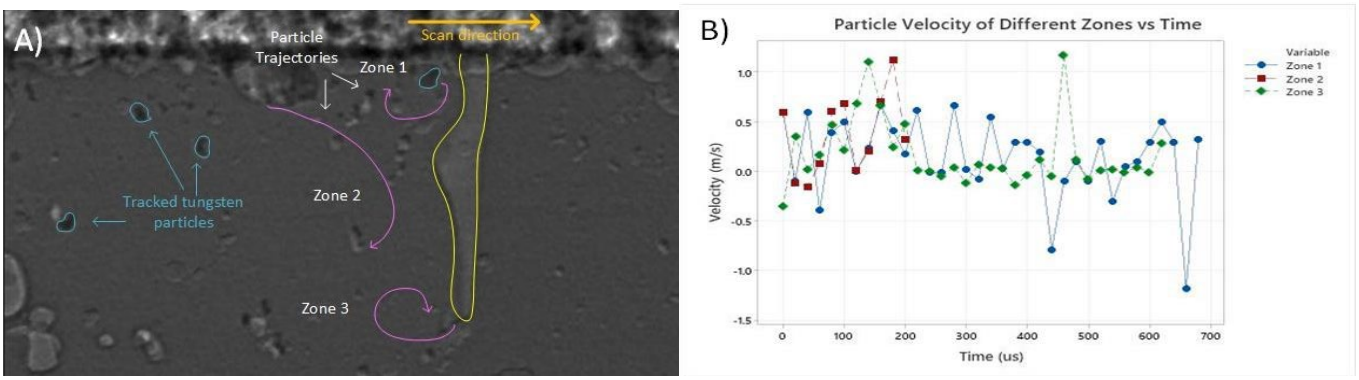


**Figure 6.** a) Visual annotation of zoning and particle tracking; b) tracked particle velocities against time

**Figure 7** shows the comparison of the different zones for experiment 173 and 189. When the particle travels backwards, this can be represented by the negative velocity on the graph. Backwards flow was mostly in part from the circular flow motion of the melt pool caused by the turbulent force of the laser and assisted by the magnetic fields on the side of the substrate. S1 is zone 1, while S2 and S3 are zone 2 and zone 3, respectively. From these graphs, it can be seen that there was more consistency in velocity deviation for zone 1 in the experiment with a magnet. It can also be seen that zone 2 had a few areas with little activity, represented by the small changes in velocity. One possibility of this occurrence could be from the lack of turbulent flow in the melt caused by the particle being too far away to be affected by it.

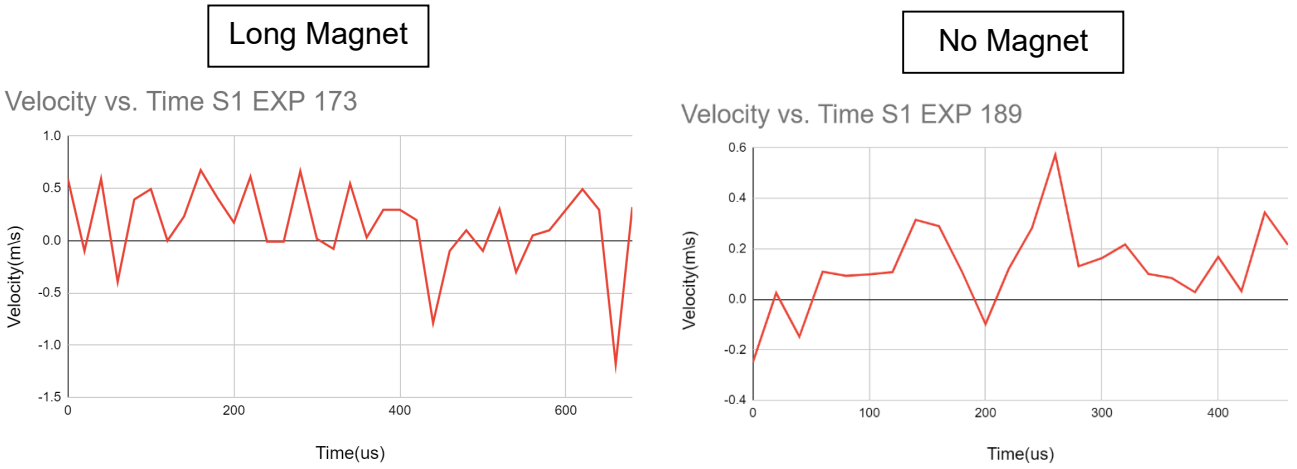

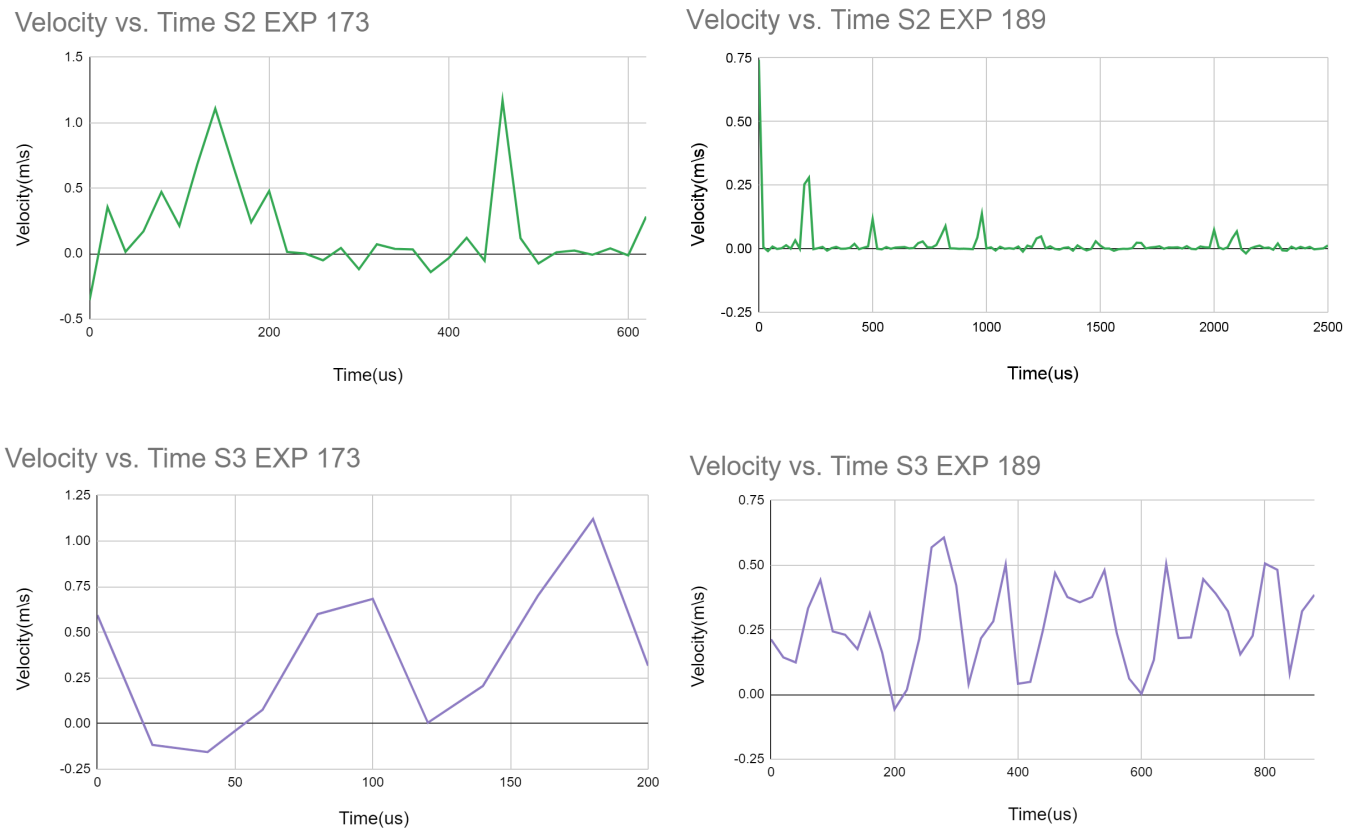


**Figure 7**. Graphs of the particles in the different zones for an experiment with a magnetic field and one without; both with line scanning process parameters; Experiment 173 was with a long magnet, experiment 189 was without a magnet

## Conclusion

Through analysis of x-ray imaging for spot welding and line scanning experiments, we are able to conclude a few different reasons behind why the melt pool characteristics change and possibly how to alter them. Our analysis was not limited to these three experiments.

From the measured keyhole depths of the three types of experiments, it was found that the ring magnet altered the experiment significantly differently than a long magnet versus no magnet with an average of 237.35 μm and 271.71 μm, respectively. With the same experiments however, it was proven that the ring magnet had no statistically significant difference when compared to the long magnet. This observation could be the result of how the magnetic fields affect certain areas of the substrate more than others. This study has proven that the magnetic fields alter the keyhole depth of the spot-welding experiments, which can be utilized for certain applications when printing parts. Simulations of these experiments could be completed, but much more time, effort, and calculations would need to be done.

With the melt pool width, it was shown that the variance was lowered for the experiments with ring magnet fields, but a lower average for the long magnet. However, the two additions of magnets produced a lower average melt pool width and variance than the experiment without a magnetic field disruption. One reason the variance was about the same for the long magnet and no magnet could be that the magnet was not having an effect on the width, which caused it to act as if there was no magnetic field present. The ring magnet could possibly alter the width of the melt pool, causing there to be less variance as an outside force was acting on the surface.

When looking at melt flow dynamics, it was found that the magnetic fields alter the velocities and trajectories of the tungsten particles within the Ti64 substrate during line scanning. It was visually seen that the particles in zone 2 and zone 1 were more sporadic than the particles in zone 3. This could be due to the magnetic field surrounding the metal, as we would expect the particles in zone 1 and 3 to behave chaotically due to the nature of the laser position. The Marangoni Flow number we calculated was found to be 12.698, which indicated a weak force from the fluid. This could be due to the magnetic field, but further analysis and tracking would need to be done to make a concrete conclusion. At the moment, it can be seen that the magnetic field has an effect on the flow of the fluid, causing abnormal stirring in the melt pool, altering the trajectories of the particles, and changing other properties like viscosity.

Future studies involve investigating how the temperature gradients are affected by the magnetic fields, and how those two combined would affect the overall process of the LBPF experiment. Another study that can be done is to look at the depth of the sub-melt pool layer and how the different types and strengths of magnets affect the size and shape of the melt pool boundary layers. Finally, another study can be done to analyze the equations used to calculate surface tension, Marangoni Flow, and settling velocity and how to alter them to adjust to the magnetic field for magnetohydrodynamic modeling. The paper presented only touches the surface on how magnetics can alter the process of additive manufacturing.

## References


1. Al-Makky, Mohammad, and Dalia Mahmoud. "The importance of additive manufacturing processes in industrial applications." *The International Conference on Applied Mechanics and Mechanical Engineering*. Vol. 17. No. 17th International Conference on Applied Mechanics and Mechanical Engineering. Military Technical College, 2016.

2. Sing, S. L., & Yeong, W. Y. (2020). Laser powder bed fusion for metal additive manufacturing: perspectives on recent developments. In *Virtual and Physical Prototyping* (Vol. 15, Issue 3, pp. 359–370). Taylor and Francis Ltd. https://doi.org/10.1080/17452759.2020.1779999

3. Sidambe, A. T. (2014). Biocompatibility of advanced manufactured titanium implants-A review. In *Materials* (Vol. 7, Issue 12, pp. 8168–8188). MDPI AG. https://doi.org/10.3390/ma7128168

4. Schneider, C. A., Rasband, W. S., & Eliceiri, K. W. (2012). NIH Image to ImageJ: 25 years of image analysis. Nature Methods, 9(7), 671–675. https://doi:10.1038/nmeth.2089

5. Aune, Ragnhild, Livio Battezzati, Rob Brooks, Ivan Egry, Hans Jörg Fecht, Jean Paul Garandet, Ken C. Mills, et al. 2005. “Surface Tension and Viscosity of Industrial Alloys from Parabolic Flight Experiments - Results of the ThermoLab Project.” In *Microgravity Science and Technology*, 15:11–14. ZARM Tec Publishing. https://doi:10.1007/bf02945937.

6. Q. Guo, “In-situ full-field mapping of melt flow dynamics in laser metal additive manufacturing,” Additive Manufacturing, vol. 31, 2020

7. E. Fereiduni, “Selective laser melting of hybrid ex-situ/in-situ reinforced titanium matrix composites: Laser/powder interaction, reinforcement formation mechanism, and nonequilibrium microstructural evolutions,” Materials Design, vol. 184, 2019.

8. Guo, Qilin, Cang Zhao, Minglei Qu, Lianghua Xiong, S. Mohammad H. Hojjatzadeh, Luis I. Escano, Niranjan D. Parab, Kamel Fezzaa, Tao Sun, and Lianyi Chen. 2020. “In-Situ Full-Field Mapping of Melt Flow Dynamics in Laser Metal Additive Manufacturing.” *Additive Manufacturing* 31 (January). Elsevier B.V. https://doi:10.1016/j.addma.2019.100939.

9. E. Fereiduni, “Selective laser melting of hybrid ex-situ/in-situ reinforced titanium matrix composites: Laser/powder interaction, reinforcement formation mechanism, and nonequilibrium microstructural evolutions,” Materials Design, vol. 184, 2019.

10. R. Wunderlich, “Surface tension and viscosity of industrial ti-alloys measured by the oscillating drop method on board parabolic flights,” High Temperature Materials and Processes, pp. 671–675, 2011.

11. D. Ershov, “Bringing trackmate into the era of machine-learning and deep-learning,” BioRxiv, 2021